A Review of Microelectronic Film Deposition Using Direct and Remote Electron-Beam-Generated Plasmas

ZENGQI YU, SENIOR MEMBER, IEEE, ZONGNAN LUO, TIEN YU SHENG, HAMID ZARNANI, MEMBER, IEEE, CHONGJIE LIN, AND GEORGE J. COLLINS, FELLOW, IEEE

Abstract—**Soft-vacuum-generated electron beams employed to create a large area plasma for assisting chemical vapor deposition (CVD) of thin films are reviewed. The electron beam plasma is used both directly, where electron impact dissociation of feedstock gases plays a dominant role, and indirectly in a downstream afterglow, where electron impact dissociation of feedstock reactants plays no role. Rather, photodissociation and metastable atom–molecule reactions dominate in the downstream afterglow. To better understand electron-beam-created plasmas using a slotted ring cathode, the transmitted beam spatial intensity profiles have been quantified from initial generation at a slotted line-shaped cold cathode through acceleration in the cathode sheath and propagation in the ambient gas. To better understand the role of photodissociation in downstream plasma-assisted CVD, the VUV output spectrum and VUV generation efficiency from electron-beam-excited plasmas have been measured. The properties of films deposited via both direct electron-beam-generated plasma-assisted CVD and downstream afterglow CVD are reviewed and compared to conventional plasma assisted CVD films.**

I. Soft-Vacuum Electron Beam Generation

A. Thermionic Sources

THE conventional means of producing electron beams uses thermionic cathode sources to emit electrons, which are accelerated in an ambient pressure typically below 10^{-4} torr. Thermionic emitters have limited application because of the low required operating pressure and the likelihood of poisoning from ambients other than inert gases. Wide area (>10 cm^2) electron beams are usually not generated from thermionic cathodes, further precluding the use of this type of source in many practical applications.

B. Glow Discharge Sources

A glow discharge environment provides a simple means to produce wide-area electron beams without the need of either thermionic sources or acceleration in high vacuum. In general, there are two groups of electrons that emerge from the cathode sheath created in a gas discharge plasma. One group contains the electrons that have undergone many inelastic collisions with gas atoms and are less energetic and isotropic in direction. Another group is comprised of energetic and highly directed electrons that have been produced at the cold cathode and accelerated perpendicular to the cathode surface. These electrons are often called beam electrons. Five established methods to create soft-vacuum electron beams from a plasma are outlined next.

1) Cold Cathodes: Electrons are emitted from a cold cathode following bombardment of the cathode by energetic species (ions, metastables, and photons) whose energy exceeds the threshold for cold electron emission, which is roughly equal to the work function of the surface for pure metal cathodes. Ion-induced secondary emission usually dominates in a discharge, and the secondary emission coefficient varies with ion species, the work function, and the Fermi energy of the cathode [1]. Cold-cathode electrons are accelerated by the electric field of the cathode, which exists in the plasma region contiguous to the cathode. Lawler *et al.* [2] have measured with laser spectroscopy the electric field in the cathode sheath of normal-glow helium plasma with a metal cathode. The electric field is linear versus distance from the cold-cathode surface, in agreement with theoretical modeling of Shi [2]. Provided we ensure a small spatial extent for the cathode fall region, few gas-phase electron-atom collisions occur as the electron traverses the sheath. Hence electrons emitted from the cathode at thermal energy can easily reach the full applied energy given by eV, where V is the cathode voltage. Energetic electrons launched into the gas subsequently create ionized and excited species when they impact ambient gas species. Some of these ionized species drift into the cathode sheath, where they are accelerated toward the cathode surface and, after impact, create secondary electrons for a sustained gas discharge.

For pure metal cathodes that have secondary emission coefficients (γ) much less than unity, the beam electrons constitute a small fraction ($<5\%$) of the total number of electrons, whereas if the cold cathode possesses a high

Manuscript received April 3, 1989; revised May 30, 1990. This work was supported in part by the Naval Research Laboratory, the National Science Foundation, Emerging Technology Division NSF Grant EET-8806851, Solid State and Microstructures, NSF Grant ECS-8906311, and the ORC Manufacturing Company, Ltd.

Z. Yu, Z. Luo, T. Y. Sheng, H. Zarnani, and G. J. Collins are with the Electrical Engineering Department, Colorado State University, Fort Collins, CO 80523.

C. Lin was on leave with the Electrical Engineering Department, Colorado State University; he is with the Department of Opto-Electronics, Chengdu Institute of Radio Engineering, Chengdu, China.

IEEE Log Number 9038307.

secondary emission coefficient ($\gamma > 1$), then the beam component can be increased to over 50%. Note that many metal-ceramic compounds, as well as pure metal cathodes with a thin native oxide, have γ's nearly ten times that of pure metal. For example, over 40% of the total discharge power is delivered to the beam electrons when using helium discharges with an aluminum cathode covered with a thin native oxide layer [3], provided sheath voltages exceed 1 kV.

2) Plasma Cathodes: A broad-area electron source was developed by Kaufman [4], based on modification of the earlier Kaufman ion source [5] by replacing the ion optics with electron optics. This source is capable of high electron beam currents (0.5-A beam current over 4-cm-diameter cross section) while operating in a 10^{-3}–10^{-5} torr environment. The energy of electrons from this source is controllable over a range from below 100 eV to over 10 keV. This source is not applicable to conventional plasma-assisted chemical vapor deposition (CVD), which requires ambient pressures between 0.1 and 20 torr.

3) Cold Cathode–Plasma Cathode Hybrids: Dugdale, and Hurley and Holliday developed a plasma-generated electron beam source where electrons are emitted from a cold cathode via secondary electron emission but where the cold cathode is surrounded by a closely spaced anode to form a volumetric plasma cathode region [6]. This device relies on tailoring the density profile of the ion space charge within the cathode sheath to both accelerate and direct the soft-vacuum electron beam. The space between anode and cathode is chosen via Paschen's law so as to avoid a discharge current via the empirically determined breakdown-voltage-versus-pressure-times anode–cathode spacing curves. Instead, the discharge occurs within the open area on the cathode, and the anode is perturbed to allow extraction of an electron beam whose cross section mirrors the aperture geometry. Discharge power densities of the order 10^6 W/cm^2 can be obtained from such a device, which operates in the 10^{-3}–1 torr pressure region.

Further improvements to cold-cathode electron guns involve the use of a beam acceleration grid, as first developed by Fusayama [7]. This device consists of a discharge cathode, an anode, and a separate acceleration grid separated by a narrow gap from the anode. The glow discharge between the cathode and anode provides a volume source of electrons which are electrostatically extracted and accelerated to form an electron beam. The electron beam energy is typically 10^2–10^3 eV, while current densities up to 0.6 A/cm^2 have been obtained in ambient pressures up to 5 torr in helium. Ranea-Sandoval *et al.* reported the generation of high-current-density (20 A/cm^2) pulsed electron beams from high-voltage (48–100 keV) glow discharges [8]. The operating pressures of these beams are from 10^{-2} to 10^{-1} torr. Finally, the pseudo-spark discharge has been used to generate intense pulsed electron beams [9].

4) Hollow-Anode Sources: Hollow-anode ion–electron sources are another approach to electron beam generation. Using a hollow-anode configuration, Miljevic [10] has generated a plasma electron source that operates at pressures from 10^{-2} to 10^{-1} torr. It provides a point or narrow slot source with millimeter minimum dimensions and an internal magnetic field that can be used to further increase the plasma density. A unique feature of this source is that a beam of either ions or electrons can be extracted.

5) Field or Barrier Emission Sources: Electrons may be directly drawn from the cathode surface by field emission when electrostatic fields in excess of 10^5 V/cm are present [11]. Hence electron beams may be obtained using a cold metal cathode placed in ultra-high vacuum with typically several hundred kilovolts applied to it. Field emission must also be considered in gas discharges when the electrode surfaces are contaminated, have sharp or irregular features, and when a thin insulating layer is present on the cathode surface. In one extreme case, one forms what has been termed a spray discharge [11], which is usually unstable and of limited practical use. Recently, Eliasson used dielectric-barrier discharges for efficient production of UV light over large areas [12]. This device is based on the "silent discharge," which is characterized by the presence of a dielectric layer within the discharge gap and short-lived microdischarges that reach current densities of a few hundred amperes per square centimeter in narrow filaments that evolve into surface discharges on the dielectric. Typical electron energies in these filaments are in the range of 1–10 eV, with electron densities on the order of 10^{14} cm^{-3}. A major advantage of this source is that it operates at high pressures up to multiatmospheric values, which is potentially well suited to plasma-assisted atmospheric CVD.

C. Our Soft-Vacuum Electron Beam Source

The wide-area soft-vacuum electron beam we employ consists of a water-cooled solid cathode and an insulating ceramic cathode shield that exposes a selected area of the cathode surface, as shown in Fig. 1(a). In practice, the front face of the cathode in Fig. 1(a) can be either slot-shaped or concave to improve discharge stability [13]. The slotted cathode is shown in Fig. 1(b) for an unwrapped ring or line source. This is a cold cathode having an insulator shield covering its outer surface and open only at the cathode slot. It is this slotted configuration that we used for our study. Current densities up to 0.5 A/cm^2 are typically obtained from cathode surfaces. This obstructed cathode operates in the abnormal glow discharge regime, where cathode voltage increases with cathode current. The electrons emitted from the shielded cold cathode by secondary emission processes are accelerated along the electric field lines in the cathode fall region, and under proper conditions a collimated electron beam is formed. The shield, or shell, is sufficiently close to prevent discharging from those surfaces of the cathode covered by the shell, as determined by the Paschen criterion. The openings in the shell define the cathode geometry from which secondary electron emission occurs. Isolated metal shells work equally well as insulating cathode shields. The anode,

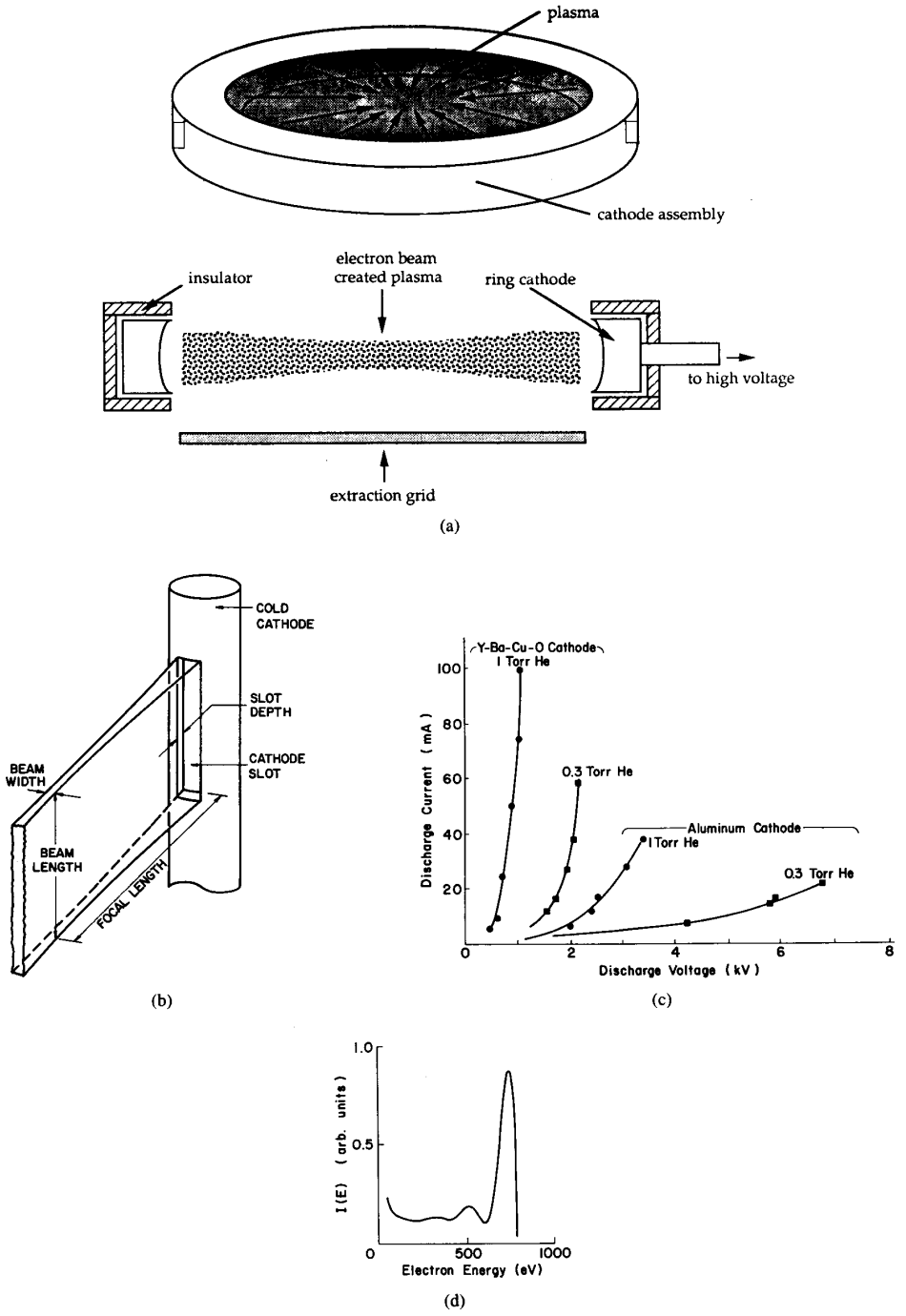

Fig. 1. (a) Three-dimensional view and cross-sectional view of disc-shaped plasma created by ring-shaped cold cathode. (b) Three-dimensional view of transverse cold-cathode electron gun with slot and associated line-shaped electron beam that is emitted. (c) *I-V* characteristics of Y-Ba-Cu-O cathode as compared with Al_2O_3 coated Al cathode. (d) Electron-beam energy spectrum emitted from Y-Ba-Cu-O cold cathode operating at 1 Torr He and 0.76 kV voltage drop across discharge.

while a necessary component of the discharge circuit, can be located anywhere within several cathode fall lengths from the cathode. Its primary function is an electron collector but, fortuitously, its placement is not crucial. Soft-vacuum electron-gun operation is generally restricted to the two gases H_2 and He. We can also use small admixtures of O_2 with the He or H_2. The O_2 helps form a thin metal oxide on a metal cathode, which acts as a high-γ

cathode material. Only when using helium or hydrogen ambient gases at pressures below 20 torr is the mean free path of the sheath electrons 5–50 times the cathode sheath dimensions. Beam generation is severely degraded in argon, neon, or xeon ambients; for example, even at pressures below 0.25 torr when using Al_2O_3 coated Al cathodes. When a metallic cathode is subjected to ion bombardment, undesired sputtering occurs and cathode impurities may be incorporated in deposited films during the CVD process. The cathode materials commonly used for the CVD experiments described herein employ either aluminum metal with a thin oxide coating or metal–metal ceramic mixtures. Each material possesses both a high secondary electron emission coefficient and a low sputter yield when operated in He or H_2 plasmas. However, other cathode materials are also useful. In the case of silicon-microelectronics-associated film deposition, silicon may be better cathode material, since it can also generate electron beams at efficiencies comparable with the sintered MgO/Mo cathode. Yet, sputtered silicon may be less of a contaminant. Composite ceramics containing barium oxide are also good cathode materials when the applications require high-electron-beam current at low-beam electron energies. For example, a Y-Ba-Cu-O cold cathode creates a low-voltage–high-current electron beam discharge as compared to the Al_2O_3-coated Al cathode shown in Fig. 1(c), which creates a low-current–high-voltage electron beam discharge. In summary, the soft-vacuum cold-cathode electron gun design is compatible with low-pressure CVD process conditions over an ambient pressure range of 10^{-1} to 30 torr.

Experimental [14] and theoretical [2], [15] studies of the generation and propagation of glow-discharge-created electron beams display an energy spectrum upper limit which corresponds to the full voltage applied to the cathode and a changing energy spectrum versus distance from the cold cathode. Electron collisions with the ambient gas act in concert to redistribute the beam electrons and form a unique energy spectrum [2]. Carman *et al.* [15] and Shi *et al.* [2] have numerically simulated the energy spectrum of soft-vacuum electron beams in a helium ambient by including elastic electron–helium collisions, electron–helium ionization collisions, electron–helium excitation collisions, superelastic collisions, and electron–electron collisions. To date, however, no studies have been reported in other, more complex gas mixtures, with the exception of $He–O_2$ mixtures [2]. The soft-vacuum electron-beam energy spectrum obtained from a Y-Ba-Cu-O cold cathode is shown in Fig. 1(d).

The wide-area (diameter 5–20 cm) disc-shaped plasma of Fig. 1(a) is well matched to planar disc substrates common to microelectronics manufacturing. To better tailor the spatial uniformity of CVD plasmas excited by a disc-shaped electron beam emitted from a ring cathode, it is important to first quantify electron beam propagation through the plasma. In the following, we provide three-dimensional spatial intensity profiles of a one-dimensional propagating wedge-shaped electron beam created by a line-shaped cold cathode containing a slot as shown in Fig. 1(b). Line-shaped slotted electron guns are easier to characterize than ring-shaped slotted guns. In the latter, trapped electron beams also occur when operating conditions allow the electron mean free path to be a significant fraction of the ring radius. Nevertheless, line beam profiles provide some valuable insight into the design of the overlapping electron beams emitted from a wide-area ring-shaped cold cathode containing a slot [13]. Of course, we realize that an understanding of line-shaped electron beam generation does not lead to a full description of the ring case. However, the beam properties in the line source greatly simplify experiments. We reemphasize that we use this same slotted line-shaped soft-vacuum electron beam source in our CVD work, but we wrap it into a slotted ring shape to create a wedge-shaped disc plasma typically 10 cm in diameter [13]. The relevance of the line source characterization is to better achieve a uniform disc-shaped plasma when the slotted line cathode is wrapped into a ring-shaped cathode.

II. Slotted Line-Source Electron Beam Characterization

A transverse cathode with a variable slot depth but a fixed 1.2-cm-wide and 15-cm-long cross section generates a broad-area wedged-shaped electron beam, as shown in Fig. 1(b). Spatial intensity profiles of soft-vacuum electron beams versus slot depth have been studied using a modified Faraday cup [14] with a spatial resolution of 0.2 mm. The measured beam profiles are best fit to Gaussian profiles, and we use the equivalent Gaussian FWHM to characterize the beam width. Care was taken to eliminate spurious currents arising from the background plasma and secondary electron production via a set of apertures placed in front of a Faraday cup, as discussed in the following. As discussed herein, the focal characteristics of the wedge-shaped beam were experimentally determined to depend strongly on the chosen slot depth. This variation of slot depth and the effect on the electron beam profile is by nature an empirical process.

For a 15-cm-long by 1.2-cm-wide slotted cathode, the intensity variation of the emitted wedge-shaped electron beam is constant to within 2% over the central 9 cm of length, regardless of the slot depth, from 0.9 to 4.7 mm. The spatial uniformity of beam current is also affected by the total cathode current, the chosen total pressure, and the gas composition. An illustrative beam intensity profile at a typical operation condition is shown in Fig. 2(a).

The focal characteristics of wedge-shaped electron beams were measured at varying operating conditions, including total $He–O_2$ ambient pressure, partial oxygen concentration, and cathode current. We define the focal length of the line source electron gun of Fig. 1(b) as the distance from the bottom of the slot cathode to the experimentally determined electron beam focal point. Minimum beam

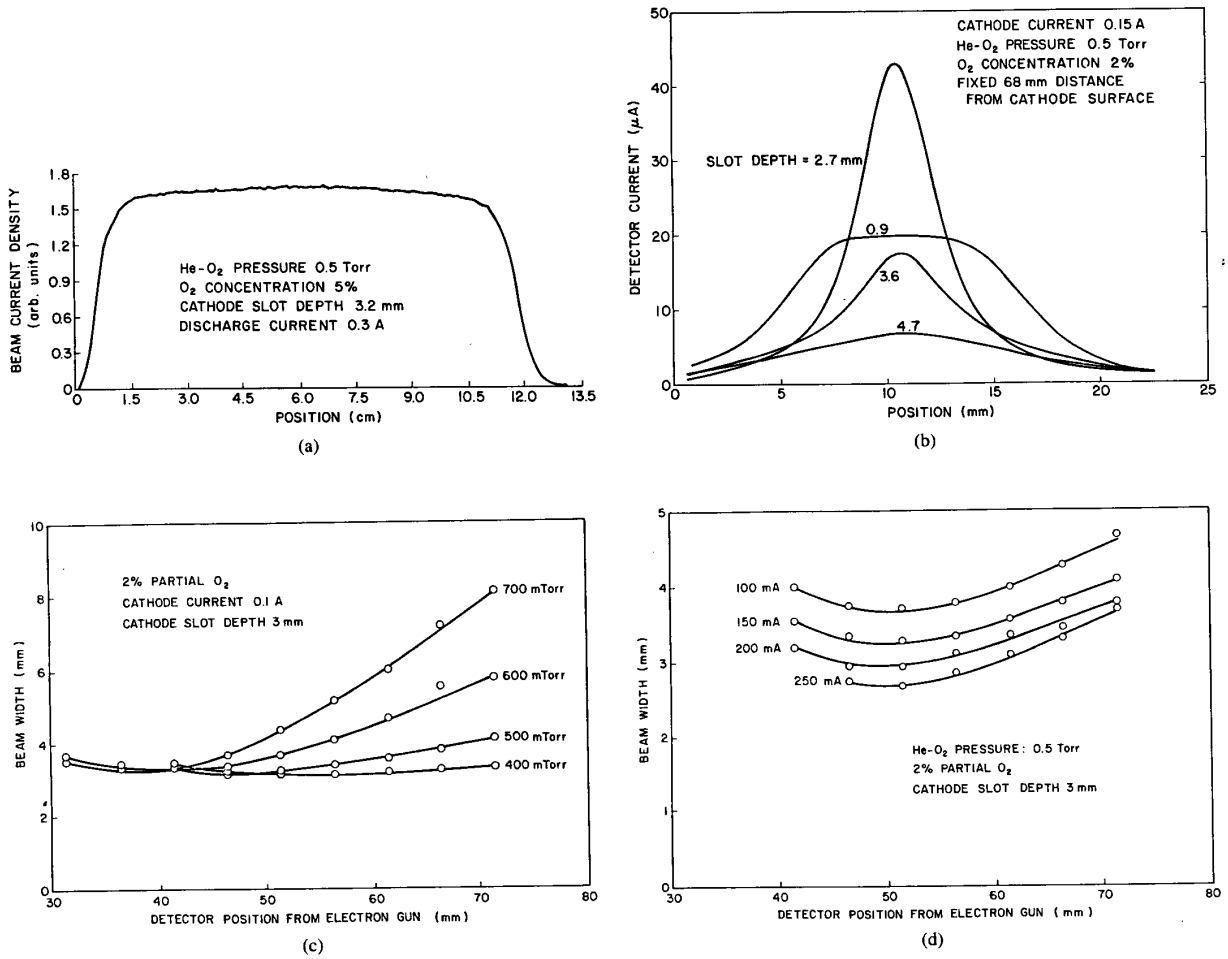

Fig. 2. (a) Line-source electron-beam intensity profile measured along beam length. (b) Line-source electron beam intensity profile across beam width with cathode slot depth as parameter. (c) Line-source beam intensity width versus detector position with total ambient pressure as parameter. (d) Line-source electron beam intensity width versus detector position with discharge current as parameter.

widths of 0.5 mm at the focal plane were demonstrated along the 10-cm active length. The beam focal characteristics were also measured, employing different cold cathode slot depths over the range 0.9–4.7 mm as shown in Fig. 2(b). At shallow (0–2 mm) cathode slot depths, the electron beam focal width is wide. This occurs because the electrostatic beam focusing, as determined via the equipotential curves of the shallow slot depth compared to the cathode sheath size, is insufficient to focus the beam. As the slot depth increases beyond the cathode sheath size, which is about 3 mm, the equipotential curves begin to follow the slot-shaped cut in the cold-cathode face, and the emitted beam begins to be electrostatically focused. In a slotted, cold cathode of variable slot depth, a trade-off exists between the desired minimum focal size and the desired focal depth. At a slot depth of 2.7 mm, we obtain a beam width of 4 mm at a 4.5-cm focal length. For slot depths of 3.6 mm, the minimum beam width further decreases, but the focal length becomes unacceptably close to the cathode face for practical applications.

In the following, we quantify focal characteristics at fixed slot depth versus total $He–O_2$ pressures and total current. First we discuss the wedge-shaped electron-beam focal characteristics for total $He–O_2$ pressures, from 400 to 700 mtorr, with other operating variables held fixed at 100 mA of cathode current, 2% oxygen in helium, and a 3-mm slot depth in the cold-cathode face. The focal length and minimum beam width versus total pressure, determined from the data in Fig. 2(c), indicate that, with increasing total pressure from 400 mtorr to 700 mtorr, the beam focal length decreases from 5.5 cm to 3.5 cm, while the minimum beam width increases only slightly. Minimum beam width is also affected by total cathode current, as shown in Fig. 2(d), from 100 mA to 250 mA, with other operating variables fixed at 500 mtorr total pressure, with 2% partial oxygen in helium, and a 3-mm-deep cold-

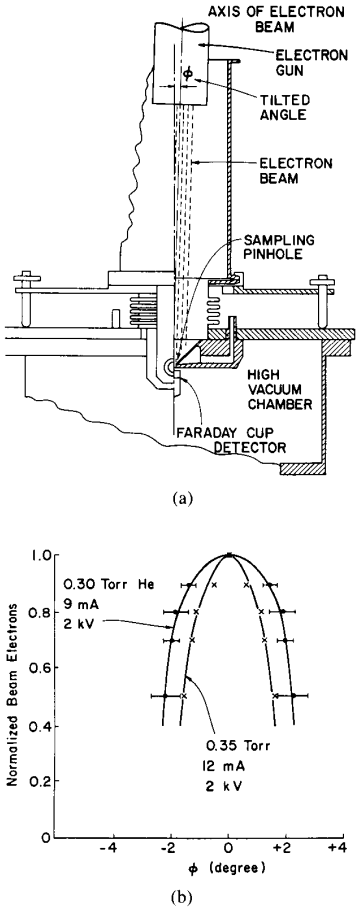

Fig. 3. (a) Schematic diagram of electron-beam intensity versus tilt-angle measurement apparatus. (b) Lateral beam profile versus angle ϕ as measured from normal to cathode surface at 4 cm from cathode.

cathode slot depth. The minimum beam width decreases with increasing cathode current while the focal length remains constant. This occurs because, at larger operating currents, the sheath dimension compared to the slot depth is unchanged and the electron energy of the beam is higher, which reduces gas-phase collisions and results in less scattering of beam electrons.

To determine the lateral divergence of the line-source soft-vacuum beam electrons as they propagate in a gaseous environment, the apparatus shown in Fig. 3(a) was used. The beam energy distribution versus angular orientation ϕ was measured using the retarding potential method [14]. The beam electron component can be computed from the derivative of detected current. An orifice of 0.2 mm in diameter was placed in front of the Faraday cup and functions as a sampling pinhole. Thus the electron beam axis is able to tilt through an angle ϕ around the sampling pinhole. Normalized beam electron intensity distributions versus ϕ for two typical operating conditions are plotted in Fig. 3(b). Beam electrons generated from the line-source cold cathode are confined within $\pm 2°$ from the normal to the cathode surface, as shown in Fig. 3(b), forming a thin plasma region. The measured FWHM of the beam electron divergence versus ϕ is about 4° at 4 cm from the cathode for a discharge voltage of 2 kV, with the helium gas pressure from 0.30 to 0.35 torr and with 9–12 mA of discharge. From Fig. 3(b), one can see that the larger the discharge current is, the narrower is the beam divergence, consistent with the data in Fig. 2(d).

III. Active Discharge and Remote Afterglow Electron-Beam-Assisted CVD (EBCVD)

Two configurations are used for soft-vacuum electron-beam-assisted CVD (EBCVD). The first utilized an active plasma with electron beams propagating either perpendicular or parallel to the substrate and feedstock gas dissociation occurring via electron impact. Two types of cold-cathode electron-beam geometries were used in the first configuration: 1) a ring-shaped cold cathode, which creates a thin disc-shaped plasma that is parallel to the substrate surface; and 2) a wide-area disc cathode, which creates a wide-area electron beam that impinges in the substrate surface. The second configuration uses a near-afterglow configuration downstream of the electron beam plasma. The feedstock gas is not exposed to the active plasma, but rather enters the afterglow, where the electron temperature is below 1.0 eV. Hence, in the afterglow configuration, feedstock dissociation occurs primarily via photodissociation or radical–molecule reactions and electron impact is negligible. Results of both types of electron-beam-assisted chemical vapor deposition (EBCVD) are compared herein to conventional plasma-enhanced CVD (PECVD) using conventional dc, radio frequency (RF), and microwave plasmas [16]. In section III-A, downstream electron-beam-created plasma CVD is presented while electron-beam-created plasma CVD is given in Section III-B.

A. Films Deposited Using Downstream Plasmas From Ring-Shaped Guns

1) Disc-Shaped VUV Lamp Characteristics and Downstream Photodissociation Studies: A ring-shaped cathode, shown in Fig. 4, emits secondary electrons following ion bombardment, metastable impingement, or the absorption of a vacuum ultraviolet (VUV) photon [13]. The secondary electrons are accelerated in the annulus cylindrical cathode sheath, thereby providing a disc-shaped electron-beam-created plasma up to 20 cm in diameter. Gas flow in Fig. 4 moves from the active plasma towards the exit port, so that a plasma plume afterglow extends from the active plasma down towards the substrate. The feedstock CVD gas species are introduced into the afterglow plasma plume downstream from the active ring

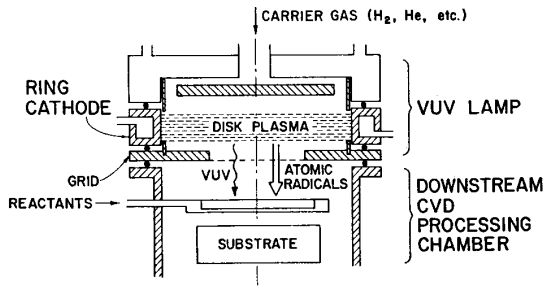

Fig. 4. Downstream plasma CVD reactor using disc-shaped electron-beam plasma for upstream plasma source.

plasma using the reactant gas inlet jet located just above the substrate, as shown in Fig. 4. Ground-state ions, metastables, or free radicals created in the confined disc plasma flow over a distance of 10 cm before reaching the substrate. The carrier gas flow is less than 10^4 cm/s, implying that the downstream plasma is more than 100 μs into the plasma afterglow and is fully thermalized. Electrons outside an applied electric field thermalize via collisions with the ambient gas within tens of microseconds to less than 1.0 eV, so electron impact plays little or no role in downstream feedstock dissociation. The upstream windowless disc plasma is primarily a source of VUV light, radical species, and excited atomic gas species, all of which can all assist dissociation of downstream CVD feedstock reactants via volume photoabsorption and excited atom–molecule as well as radical–molecule collisions, respectively. In addition, the excited radical flux and VUV impingement on the film may also assist heterogeneous surface reactions and increase surface mobility of absorbed species.

In the near afterglow hydrogen or helium gas disc plasma, nearly 10% of the discharge power is measured to go into VUV photons, and we estimate that nearly half the discharge power creates atomic radicals, ions, and metastables which interact downstream with feedstock gases. Excited atoms (e.g., He or H) within the disc-shaped electron-beam-created plasma emit VUV radiation primarily on their resonance lines. Because the spatial thickness of the beam-created disc plasma is much thinner (3–6 mm width) as compared to that of conventional plasmas (several cm). The resonant photon mean-free path is comparable to the lamp plasma thickness rather than being much less. Hence resonance trapping of VUV photons emitted by atomic species is minimized in the thin plasma disc. That is, atomic hydrogen does not cause appreciable self-absorption inside the several-millimeter-thick disc plasma. The Lyman alpha emission ($2p\ ^2P^0 - 1s\ ^2S$) at a wavelength of 121.6 nm dominates the emission spectra when running a H_2 discharge, while the N I line ($3s\ ^4P - 2p\ ^4S^0$) at 120.0 nm dominates the emission spectra in a N_2 discharge. Moreover, atomic hydrogen resonance radiation at $\lambda = 121$ nm emitted from the hydrogen disc plasma can propagate far from the disc-shaped plasma since molecular hydrogen outside the plasma does not significantly absorb 121-nm photons. Clearly, resonance absorption effects outside the disc plasma for atomic helium emission are quite different from those of atomic H, since outside the disc plasma, atomic helium absorbs resonant light over a much longer path. In fact, we observe that at the substrate, which is 10 cm from the active plasma, the He II VUV spectra dominates over the He I VUV spectra because the He I resonance lines, at 58 nm, emitted from the plasma disc, are resonantly absorbed, and the intensity of 58-nm radiation is rapidly diminished with distance from the disc. Ionized He spectra emitted from the disc plasma, however, do not suffer the resonance self-absorption of neutral helium since the He ion ground-state density outside the disc plasma is small. As a consequence, the He II spectra dominate over the He I spectra when intensity measurements are made 10 cm from the active plasma.

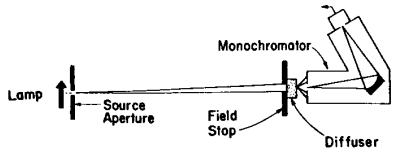

Fig. 5. Schematic diagram of VUV radiance calibration procedure (see reference [17]).

The intensity of VUV emission at 121 nm from the central 15 cm of the 20-cm diameter hydrogen plasma has been quantified by using a 0.2-m monochromator (ARC model VM 502) calibrated by the emission from a Pt–Ne hollow cathode lamp (Westinghouse Electric Corp., WL-34045) used as a secondary radiance standard. The calibration setup is shown in Fig. 5 using a Pt-Ne hollow cathode lamp having a MgF_2 window. The detailed calibration procedure can be found in [17] as reported by Ott *et al.* of the National Institution of Standards and Technology. A LiF window material ground on one side is used as the diffusing element, located 2 cm in front of the entrance slit of the monochromator to eliminate undesired angle dependence of the detection system. The field stop used is 3.2 mm in diameter and is placed adjacent to the LiF diffuser. The source aperture, 2.3 mm in diameter, is located 90 mm away from the field stop. This source aperture is placed next to the disc plasma when operating with the plasma lamp, or is placed in the front opening of the hollow cathode Pt-Ne lamp. A VUV line radiance of 1.6×10^{-3} W · cm^{-2} Sr^{-1} is obtained from a disc H_2 plasma at 0.5 torr excited by 50-mA discharge, or a VUV radiance of 9.2×10^{-3} W · cm^{-2} Sr^{-1} from a 1-torr H_2 disc plasma excited at 300 mA. This VUV flux corresponds to 6–10% of the total discharge power going into VUV light output. The intensity uniformity of VUV emission from this wide-area lamp is measured to be $\pm$ 6% using either atomic helium, molecular N_2, or H_2.

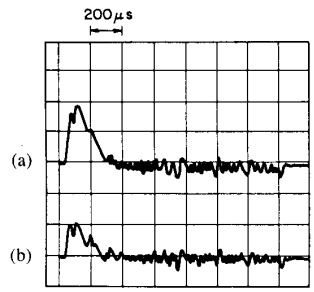

Fig. 6. Time evolution. (a) Of discharge current pulse corresponding to 121.6-nm emission of atomic hydrogen. (b) Of 417.2-nm emission of atomic Ga, following introduction of TMGa into downstream plume of disc plasma lamp.

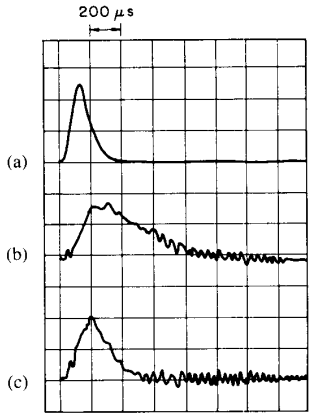

Fig. 7. Time evolution. (a) Of discharge current pulse corresponding with 121.5-nm emission of He. (b) Of 632.8-nm emission of NeI. (c) Of 417.2-nm emission of GaI, from downstream plume of disc plasma lamp.

Next we follow a specific illustrative example of VUV photodissociation of trimethylgallium (TMGa) in the near-afterglow reactor so as to emphasize the importance of VUV photodissociation under our remote plasma CVD conditions. A more detailed discussion is found in [20].

As shown in Fig. 4, the TMGa reaction zone was located 10 cm downstream from the active plasma. Spatial- and time-resolved studies of decomposition of TMGa by the disc plasma, operating in the pulsed discharge mode, have helped to partially unravel and define the primary mechanisms of downstream feedstock gas dissociation. Pulsed operation of the disc plasma allows for well-defined separation in time of VUV photon- versus radical-driven dissociation pathways. Following the ignition of pulsed active plasma, the time required for the VUV radiation emitted in the active plasma to propagate to the reaction zone is less than several nanoseconds. In contrast, the atomic radical species created in the upstream plasma require hundreds of microseconds to reach the reaction zone because the particle flow is much slower. Hence time-resolved optical emission studies from known dissociation products created in the reaction zone help to identify direct photodissociation reaction pathways of TMGa from two-body radical–TMGa collisions. Each process has unique products and unique timeframes associated with it.

In our study, a pulse power supply (Velonex model 350) ignited a 100-μs duration discharge within the plasma disc of Fig. 4 with a repetition rate of 300 Hz. A downstream optical detection system collected light emitted from the reaction zone. Fig. 6(a) displays the time evolution of the current pulse to the active plasma which is shown to be coincident with 121.6 nm VUV photoemission from active plasma discharge. Based upon the thermodynamic value of the bonding energies in TMGa [18], a 121.6-nm single photon has adequate energy to remove all three methyl radicals, even if excited to a repulsive potential surface. Fig. 6(b) shows the synchronous variation of the atomic gallium (GaI) emission line at 417.2 nm with the 121.6-nm photon flux. This is consistent with 121.6-nm photons initiating the TMGa dissociation process and causing dissociation of TMGa rather than downstream hydrogen radicals. Subsequently, a two-component optical window was used to cover the port connecting the upstream plasma to the downstream deposition chamber of Fig. 4, to create a tandem lamp and CVD chamber separated by two distinct windows. One window was made of MgF_2 capable of transmitting the 121.6-nm radiation, while the second was made of Pyrex glass, which is opaque to 121.6-nm photons. Gallium deposits were formed on the window side facing toward the CVD chamber, but only for the MgF_2 window, not for the glass window. This provides further direct evidence that 121.6-nm photons play a direct role in dissociating TMGa in a downstream hydrogen plasmas.

Fig. 7(a) shows the time evolution of the current pulse to the active helium plasma which is synchronous with the VUV emission from the helium discharge. We introduced neon into the downstream plasma, and where it entered the afterglow plume we observed a distinct red glow. Fig. 7(b) shows the intensity of the neon (NeI) 632.8-nm transition known to be pumped by the helium 2^1S metastable [19] via metastable helium-ground-state neon collisions. We did not determine the helium 2^1S or 2^3S density. The observed time delay corresponds to the expected velocity of gas flow in our flowing afterglow reactor. The helium metastable species (2^3S and 2^1S) flow into the reaction volume from discharge region with a time delay of nearly 200 μs, as shown in Fig. 7(b). The He (2^3S) density usually predominates over the He(2^1S) density due to the importance of superelastic collisions [19]. The presence of a large He 2(^1S) density confirms our near-afterglow (Δt = ms), where the He (2^1S) density is negligible. Fig. 7(c) shows the emission signal measured from the atomic Ga I line following TMGa dissociation in the downstream region of the remote helium plasma. Note that the peak Ga emission occurs in-between the measured peaks for

TABLE I
DISC PLASMA DOWNSTREAM CVD OPERATION CONDITIONS

Films	AlN	a-Si:H
Source	H_2 plasma H: 121.6 nm	He plasma He^+: 121.5
Cathode current	0.2 A	0.5 A
Cathode voltage	500 V	600 V
Reactant	TMA/NH_3	Si_2H_6
Gas flow	1/40 NH_3 60 SCCM H_2 200 SCCM	 Si_2H_6 20 SCCM He 200 SCCM
Total pressure	1 torr	1–1.5 torr
Substrate temp.	100°–400°C	50°–400°C
Deposition rate	60–200 Å/min	>200 Å/min

TABLE II
PROPERTIES OF AlN FILMS

	Disc-Plasma CVD	193-nm Laser CVD
Refractive index	1.7–2.0 (100°–400°C)	1.7–1.9 (200°–400°C)
Dielectric constant (at 1 MHz)	7.5–8.0	7.0–8.0
Breakdown voltage (MV/cm)	2–4 (200°–400°C)	2–3 (300°–400°C)
Resistivity ($\Omega \cdot$ cm)	5×10^{13} (400°C)	10^{13} (400°C)
Wet etch rate (Å/s at H_3PO_4)	460–50 (100°–400°C)	500–100 (200°–400°C)
Relative NH bonding concentration ($\alpha \Delta H$) from FTIR (arb.unit)	0.1–0.1 (100°–400°C)	1.0–0.1 (200°–400°C)

the helium VUV emission and for the $He(2^1S)$ driven neon emission. This time behavior indicates that in helium afterglows both VUV photodissociation and two-body helium metastable-TMGa collisions contribute to the decomposition of TMGa [20].

2) Disc Plasma and Downstream Film Deposition: Thin films of aluminum nitride and hydrogenated amorphous silicon have been deposited at substrate temperatures between 100°C and 400°C. The deposited films show significant improvement over other CVD processes in the film quality achieved, the substrate temperature required, and the maximum deposition rates achieved.

Amorphous silicon and aluminum nitride films have been deposited in the downstream afterglow of either helium or H_2 when using Si_2H_6, TMA, and NH_3 feedstock gases, respectively. Typical afterglow deposition conditions for the two film depositions are listed in Table I.

Aluminum nitride thin films (AlN) are deposited on three substrates: heavy metal fluoride glass (HMF), silicon wafers, and III–V wafers. CVD feedstock gases employed are trimethylaluminum (TMA) and ammonia (NH_3) [21]. The feedstock reactants are both photo dissociated and decomposed via excited hydrogen atom–molecule reactions such as $H^* + TMA \rightarrow$ collisional dissociation products. Details of TMA and NH_3 photodissociation pathways have been studied previously [22]. The deposition rate varied from about 200 Å/min for a 400°C substrate temperature to about 60 Å/min for a 100°C substrate temperature.

The AlN film properties measured include refractive index, film resistivity, and dielectric constant (see Table II), in comparison with the films deposited by excimer-laser-assisted CVD. It is especially noteworthy that with this near afterglow disc plasma we can deposit high-quality AlN films at 100°C, whereas the laser CVD technique is not able to do so below 200°C. The deposited film thickness variation with near-afterglow deposition is within 5% over a 10-cm diameter substrate. The wet etch rate at 60°C of disc plasma deposited AlN in 85% phosphoric acid (H_3PO_4) was also examined. The near-afterglow disc plasma method deposited AlN films that show a two to three times lower etch rate than laser-deposited films, indicating both a lower hydrogen content and a higher film density. The refractive index of deposited AlN films was measured to be 2 at 400°C substrate temperature and is comparable to excimer-laser-deposited AlN, which has a refractive index of 1.9 for a 400°C deposition temperature [23]. Moreover, AlN deposited at 400°C with the disc plasma downstream CVD exhibits a resistivity similar to that reported for bulk AlN ($\geq 5 \times 10^{13}$ Ω cm) [24].

The deposited AlN film was examined using complementary Auger electron spectroscopy and infrared absorption spectroscopy to determine the elemental Al/N ratio and the total amount, as well as the specific chemical form of hydrogen bonding. Disc plasma and laser-assisted CVD films have nearly equivalent aluminum to nitrogen ratios. However, the total hydrogen content of disc-plasma deposited AlN films are low at all substrate temperatures. In

TABLE III
PROPERTIES OF a-Si:H FILMS

	Disc Plasma	193-nm Laser	RF Plasma
Photoconductivity (Ω^{-1} cm^{-1})	4×10^{-4}	1.2×10^{-5}	1×10^{-3}
Dark conductivity (Ω^{-1} cm^{-1})	3.5×10^{-9}	2.5×10^{-11}	3×10^{-9}
Optical band gap (eV)	1.76	1.7	1.7–1.8
Conductivity activation energy (eV)	0.71	0.85	0.76
Refractive index	3.62	3.5	3.43
Hydrogen concentration (%)	4.3	12	14

TABLE IV
CHEMICAL PROPERTIES OF CVD SiO_2

	Electron Beam	RF Plasma [35]
Stoichiometry	SiO_2	$SiO_{1.94}N_{0.06}$
Nitrogen (%)	<1	3
Carbon (%)	<2	0.1
Hydrogen bonding		
2270 cm^{-1} SiH (%)	<1	2
3380 cm^{-1} H_2O (%)	<0.001	<0.001
3650 cm^{-1} OH (%)	<0.01	0.002

TABLE V
PHYSICAL PROPERTIES OF CVD SiO_2

	Electron Beam	RF Plasma [35]
Adhesion (10^8 dyne/cm^2) (1000 Å on Si)	>7	>7
Refractive index (6328 Å)	1.46	1.46
Stress on Si_2 (compressive) (10^9 dyne/cm)	9.4	3.6

contrast, the hydrogen bonding in laser CVD AlN films increases over one order of magnitude when the substrate temperature is lowered to 200°C from 400°C. Note that at 400°C the hydrogen concentration has the same level for both laser and disc-plasma deposited films. The hermetic properties of hydrogen disc-plasma-deposited AlN films on HMF glass were examined by the chemical leach rate method. The leach rate of the HMF samples coated using disc-plasma-assisted CVD of AlN is $\sim 10^{-6}$ PPM/min, indicating a hermetic film consistent with the low hydrogen content, high density, and low etch rates.

In conclusion, the downstream hydrogen-plasma-assisted CVD achieves higher quality AlN films at lower substrate temperature than prior art excimer-laser CVD methods [23].

The disc plasma employing helium as a carrier gas was used for deposition of hydrogenated amorphous silicon, using disilane as a feedstock on crystalline silicon wafers or glass substrates. Helium is introduced upstream to the disc plasma, and in addition to He VUV radiation, plasma products created in the disc-plasma (He^+, He 2^1S, He 2^3S) flow downstream toward the substrate at thermal kinetic energy. The hydrogenated amorphous silicon films deposited by disc-helium-plasma dissociation of disilane have film properties comparable to the films deposited using excimer lasers or RF plasma, as shown in Table III. Typically a film deposited at a substrate temperature of 350°C has a refractive index of 3.62, an optical band gap of 1.76 eV, a photoconductivity of $4 \times 10^{-4}\,(\Omega \cdot \text{cm})^{-1}$, and a dark conductivity of $3.5 \times 10^{-9}\,(\Omega \cdot \text{cm})^{-1}$. The conductivity activation energy was measured to be 0.71 eV. The optoelectronic properties of Table III are comparable with that of RF plasma films [25]. The hydrogen concentration, bonded only as Si–H for our films, is found to vary from 4 to 8% as the substrate temperatures varies from 350°C to 300°C.

B. Active Electron Beam Plasma-Assisted CVD of SiO_2, Si_3N_4, and $SiO_xN_yH_z$ Films

Electron-beam-assisted chemical vapor deposition (EBCVD) uses a line source electron gun to excite the active plasma [26], [27]. In this configuration the electron beam travels parallel to, and a few millimeters away from, a heated substrate, creating a confined electron-beam

TABLE VI
ELECTRICAL PROPERTIES OF CVD SiO_2

	Electron Beam	RF Plasma [35]
Breakdown voltage (MV/cm)	2-3	10
Resistivity at 1 MV/cm ($\Omega \cdot$ cm)	10^{14}-10^{16}	10^{16}
Flatband voltage (V)	0.5-3	<0.2
Dielectric constant at 1 MHz	3.5	4.6

TABLE VII
CHEMICAL PROPERTIES OF CVD Si_3N_4

	Electron Beam	RF Plasma [36]
Stoichiometry	Si_3N_4	Si_3N_4
Oxygen (%)	<0.1	<1
Carbon (%)	<0.1	<1
Hydrogen bonding by FTIR		
Si-H (%)	<0.1	12-16
N-H (%)	8-10	2-7

TABLE VIII
PHYSICAL PROPERTIES OF CVD Si_3N_4

	Electron Beam	RF Plasma [36]
Adhesion (10^8 dyne/cm^2) (1000 Å on Si)	>5.5	>6
Refractive index (6328 Å)	1.85	2

TABLE IX
ELECTRICAL PROPERTIES OF CVD Si_3N_4

	Electron Beam	RF Plasma [36]
Breakdown voltage (MV/cm)	5	4
Resistivity at 1 MV/cm ($\Omega \cdot$ cm)	10^{15}	10^{15}-10^{16}
Dielectric constant at 1 MHz	7.1	7

plasma volume that also scatters energetic electrons onto the film during film growth. Alternatively, a wide-area disc plate cathode is also used to create a wide-area electron beam traveling perpendicular to the substrate when deposition occurs. A molybdenum plate heated by a 500-W tungsten halogen lamp, in combination with a thermocouple and temperature controller, provides a regulated substrate temperature from 50°C to 500°C. In either case, electron impact on feedstock gases causes dissociation, and products condense on the substrate to form a film.

SiO_2 and Si_3N_4 film properties deposited using either the wedge-shaped plasma parallel to the substrate surface or films deposited using the wide-area electron beam traveling perpendicular to the substrate are summarized in Tables IV-IX [26]-[34]. The film properties of EBCVD are also compared with conventional RF plasma [35], [36] deposited films. Deposition conditions are chosen to be similar except for the higher gas flow ratio and lower total pressure for EBCVD to ensure complete reaction of the reactants. Deposition rates of 500 Å/min and 200 Å/min are achieved for SiO_2 and Si_3N_4 films, respectively, for EBCVD compared to the ~300 Å/min for RF CVD. We employed 250°-400°C substrate temperatures to achieve acceptable film properties. The physical, chemical, and electrical properties of SiO_2 and Si_3N_4 films possess the following major features, listed in Tables IV-IX. The index of refraction of EBCVD SiO_2 films is close to the thermally grown SiO_2 value of 1.46. Conformal step coverage over 5000-Å aluminum and polysilicon patterns has been demonstrated for the EBCVD SiO_2 films [30]. The EBCVD films Si_3N_4 films are oxygen- and carbon-free within the limits of Auger detection (1%) when using NH_3 and nitrogen-diluted SiH_4 as reactants. The Si-H bonding from infrared absorbance measurements in EBCVD Si_3N_4 films is remarkably low. Besides the unique features described in the preceding, most of the properties of EBCVD films are comparable to that of conventional RF plasma CVD films.

IV. CONCLUSION

Plasma-generated soft-vacuum electron beams have been used to create both active and remote plasmas of wide area to assist CVD of thin films. The active electron-beam plasma utilizes beam electrons for feedstock gas decomposition while the near afterglow plasma primarily provides VUV photons, excited species, and metastable species which dominate the feedstock gas dissociation processes. Direct electron impact processes play a minor role because backstreaming of reactions is negligible under our flow rates. A primary benefit of the near-afterglow method is that it reduces charged particle bombardment damage to the depositing films. The electron beam intensity profile from a slotted line-source cathode was measured as a guide to understanding the slotted ring cathode source. Focal characteristics were determined as a function of cold cathode geometry and discharge conditions and the empirical results used to design a more uniform disc-shaped plasma excited by a slotted ring. Electron-beam-assisted deposition of SiO_2, Si_3N_4, amorphous silicon, and AlN films provides films whose physical, chemical, and electrical properties are comparable to those obtained from other plasma-assisted methods.

REFERENCES

[1] P. Zalm and L. Beokers, *Surf. Sci.*, vol. 152, p. 135, 1985.
[2] For electric field measurements in the sheath, see E. A. DenHartog, D. A. Doughty, and J. E. Lawler, *Phys. Rev. A.*, vol. 38, no. 5, p. 2471, 1988; for calculations of the effect of a linear electric field, see B. Shi, J. Meyer, Z. Yu, and G. J. Collins, *IEEE Trans. Plasma Sci.*, vol. PS-14, no. 4, p. 523, 1986, and B. Shi, G. J. Fetzer, Z. Yu, and G. J. Collins, *IEEE J. Quant. Electron.*, vol. 21, p. 265, 1989.
[3] J. Rocca, J. Meyer, M. Farrell, and G. J. Collins, *J. Appl. Phys.* vol. 56, no. 3, p. 790, 1984.

[4] H. R. Kaufman, *J. Vac. Sci. Technol.*, vol. A3, no. 4, p. 1774, 1985.
[5] H. R. Kaufman and R. S. Robinson, *AIAA J.*, vol. 20, no. 6, p. 745, 1982.
[6] R. A. Dugdale, *J. Mater. Sci.*, vol. 10, p. 896, 1975; and R. E. Hurley and J. H. Holliday, *Vacuum*, vol. 28, nos. 10/11, p. 453, 1978.
[7] M. Fusayama, *J. Appl. Phys.*, vol. 25, no. 5, p. L406, 1986.
[8] H. F. Ranea-Sandoval *et al.*, *IEEE Trans. Plasma Sci.*, vol. PS-15, no. 4, p. 361, 1987.
[9] W. Benker, J. Christiansen, K. Frank, H. Gundel, W. Hartman, T. Redel, and M. Stelter, *IEEE Trans. Plasma Sci.*, vol. 17, p. 754, 1989.
[10] V. I. Milijevic, *J. Appl. Phys.*, vol. 63, no. 7, p. 2237, 1988; and V. I. Milijevic, *Rev. Sci. Instrum.*, vol. 55, no. 6, p. 931, 1984.
[11] R. J. Noer, *Appl. Phys.*, vol. A28, no. 1, 1982; and R. A. Millikan and C. F. Eyring, *Phys. Rev.*, vol. 27, no. 51, 1926, and C. F. Eyring, S. S. Mackeown, and R. A. Millikan, *Phys. Rev.*, vol. 31, p. 900, 1928; see also M. J. Druyvesteyn and F. M. Penning, *Rev. Mod. Phys.*, vol. 12, no. 87, 1940.
[12] B. Eliasson and V. Kogelschatz, *Appl. Phys.*, vol. B46, p. 299, 1988.
[13] G. J. Collins and Z. Yu, U.S. Patents 4 782 267 and 4 509 451.
[14] J. Mizeraczyk, *J. Phys. D*, vol. 17, p. 1647, 1984; P. Gill and C. E. Webb, *J. Phys. D: Appl. Phys.*, vol. 10, p. 299, 1977; Z. Yu, J. J. Rocca, and G. J. Collins, *J. Appl. Phys.*, vol. 54, no. 1, p. 131, 1983; and R. M. Chaudhri and M. M. Chaudhri, in *Int. Conf. Phenomena Ionized Gases* (Belgrade), 1965, vol. 1, p. 392.
[15] R. J. Carman and A. Maitland, *J. Phys. D: Appl. Phys.*, vol. 20, p. 1021, 1987.
[16] P. K. Bachmann, G. Gartener, and H. Lydtin, *MRS Bulletin*, vol. 13, no. 12, p. 52, 1988.
[17] W. R. Ott, J. M. Bridges, and J. Z. Klose, *Opt. Lett.*, vol. 5, no. 6, p. 225, 1980.
[18] D. G. Tuck, in *Comprehensive Organometallic Chemistry*, G. Wilkinson, G. A. Stone, and E. W. Abel, Eds. Oxford: Pergamon Press, 1982, 684 pp.
[19] E. E. Bewton, E. E. Furgason, F. A. Matson, and W. W. Robertson, *Phys. Rev.*, vol. 128, p. 206, 1962; see also, A. V. Phelps, *Phys. Rev.*, vol. 99, p. 1307, 1985.
[20] T. Sheng, B. Pihlstrom, and Z. Yu, *Appl. Phys. Lett.*, vol. 55, p. 2411, 1989.
[21] T. Y. Sheng, Z. Yu, and G. J. Collins, *Appl. Phys. Lett.*, vol. 52, p. 576, 1988.
[22] D. J. Ehrlich, R. M. Osgood, Jr., and T. F. Duetsch, *IEEE J. Quantum Electron.*, vol. QE-16, p. 1233, 1980; see A. W. Laubengayer, J. D. Smith, and G. G. Ehrlich, *Amer. Chem. Soc.*, vol. 83, p. 542, 1961; see V. M. Donnelly, A. P. Barowavski, and J. R. McDonald, *Chem. Phys.*, vol. 213, p. 218, 1979; see also D. Eres, T. Motooka, S. Gorbatkin, D. Lubben, and J. E. Greene, *J. Vac. Sci. Technol.*, vol. B5 p. 848, 1987.
[23] C. A. Moore, Z. Yu, L. R. Thompson, and G. J. Collins, in *Handbook of Thin Films Deposition Processes and Technologies*, K. Schuegraf, Ed. Park Ridge, NJ: Noyes, 1988, chap. 10.
[24] Y. Kurokawa, K. Utsumi, H. Takamizawa, T. Kamata, and S. Noguchi, *IEEE Trans. Compon. Hybrids Manuf. Technol.*, vol. CHMT-8, p. 247, 1985; see also M. Hirose, *Semiconductors and Semimetals*, vol. 21, part A, J. I. Pankove, Ed. New York: Academic, 1984.
[25] H. Zarnani, Z. Yu, G. J. Collins, E. Bhattacharya, and J. I. Pankove, *Appl. Phys. Lett.*, vol. 53, p. 131, 1988.
[26] L. R. Thompson, J. J. Rocca, K. Emery, P. K. Boyer, and G. J. Collins, *Appl. Phys. Lett.*, vol. 43, p. 777, 1983.
[27] Z. Yu, J. J. Rocca, J. D. Meyer, and G. J. Collins, *J. Appl. Phys.*, vol. 53, p. 4704, 1982.
[28] P. K. Boyer, G. A. Roche, W. H. Ritchie, and G. J. Collins, *Appl. Phys. Lett.*, vol. 40, p. 716, 1982.
[29] H. E. Maes *et al.*, presented at the 1983 Meeting Electrochemical Society—Compound Semiconductors, Plasma Nitrides, San Francisco, CA, May 8–13, 1983.
[30] L. R. Thompson *et al.*, *J. Electrochem. Soc.*, vol. 131, no. 2, p. 462, 1984.
[31] H. J. Stein, V. A. Wells, and R. E. Hampy, *J. Electrochem. Soc., Solid-State Sci. Technol.*, vol. 126, p. 1750, 1979.
[32] W. Pliskin, *J. Vac. Sci. Technol.*, vol. 141, p. 1064, 1977.
[33] H. Dunn, P. Pan, F. R. White, and R. W. Douse, *J. Electrochem. Soc.*, vol. 128, p. 1555, 1981.
[34] B. Zhang, T. Hwang, W. H. Ritchie, Z. Yu, and G. J. Collins, *J. Vacuum Sci. Technol.*, vol. A7, no. 2, p. 176, 1989.
[35] K. Emery *et al.*, SPIE Session 459-02, Los Angeles, CA, 1984; R. M. Levin, *J. Vac. Sci. Technol.*, vol. B1, p. 54, 1983; P. K. Boyer, *Appl. Phys. Lett.*, vol. 40, p. 716, 1982.
[36] R. S. Rosler and G. M. Engle, *Solid State Technol.*, vol. 24, no. 5, p. 172, 1981.

*

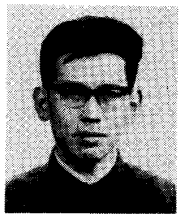

Zengqi Yu (SM'89) was born in China on November 26, 1941. He received the degree in physics from Fudan University, Shanghai, and received the M.S. and Ph.D. degrees in electrical engineering from Colorado State University, Fort Collins, CO.

He was teaching and performing experimental research at Fudan University during 1965–1984, and has been doing research at Colorado State University since 1980. His research interests are in soft-vacuum electron-beam sources and their applications to microelectronic film processes, gas lasers, metal vapor ion lasers, laser ablation for film coating, magnetron sputtering for fiber coating, plasma physics, spectroscopy, and vacuum physics.

Dr. Yu is a member of several academic societies.

*

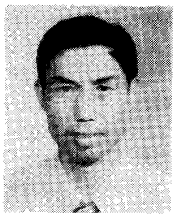

Zongnan Luo was born in Jiangsu, China, on October 12, 1940. He received the B.S. degree in electrical engineering from the Nanjing Institute of Technology, China, in 1963.

His research area is gas discharge, lasers, and optoelectronic detecting technique. He joined the Electrical Engineering Department at Colorado State University, Fort Collins, in 1987 as a Visiting Scholar, involved in the research of plasma-generated electron-beam characterization and application.

*

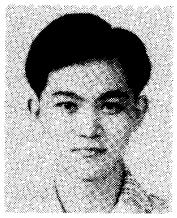

Tien Yu Sheng was born in Taiwan on June 1, 1958. He received the B.S. degree in physics from National Tsin-Hua University in Taiwan in 1981, and the M.S. degree in physics from Colorado State University, Fort Collins, in 1989, where he is now a Ph.D. candidate, studying energetic assisted MOCVD of semiconductor thin films.

*

Hamid Zarnani (S'82-M'86) was born in Zanjan, Iran, on January 21, 1954. He received the B.S. degree in physics from the University of Joundi-Shapour, Ahvaz, Iran, in 1977, and the M.S. degree in electrical engineering from the University of Bridgeport, Bridgeport, CT, in 1982.

He is currently a Ph.D. candidate in the Electrical Engineering Department of Colorado State University (CSU), Fort Collins, CO. He has been with CSU since 1988 as a Research Associate,

working in the area of laser and plasma processing of microelectronic thin films. Currently, he is working on laser and VUV lamp processing of YBaCuO superconductor thin films.

Mr. Zarnani is a member of the American Physical Society (APS), the Optical Society of America (OSA), SPIE, and the Material Research Society (MRS).

*

Chongjie Lin was born in China on May 21, 1938. He visited Colorado State University in 1988-1989 as a Visiting Scholar.

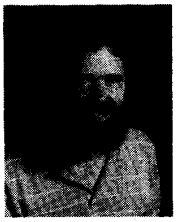

George J. Collins (S'62-M'72-SM'75-F'87) graduated from Yale University, New Haven, CT.

He is a Professor of electrical engineering at Colorado State University, Fort Collins. He has served as a Consultant to both industry and government, including Bell Laboratories, NCR, Lawrence Livermore National Laboratory, and the National Bureau of Standards, Lasertechnics (Albuquerque, NM), and the Applied Electron Corporation (Santa Clara, CA). Prior to joining Colorado State University, he was a Research Associate at the Dunham Laboratory, Oxford University, and a Visiting Scientist under the U.S.-Japan Cooperative Science Program at Nagoya University. He is the author of more than 100 technical papers.

Dr. Collins is a member of the American Physical Society, Eta Kappa Nu, and Sigma Xi. He is a Sloan Foundation Fellow (physics) and is a recipient of the Halliburton Award.